JGR Oceans

RESEARCH ARTICLE
10.1029/2019JC015056

Special Section:
The Three Major Hurricanes of 2017: Harvey, Irma and Maria

Copolarized and Cross-Polarized SAR Measurements for High-Resolution Description of Major Hurricane Wind Structures: Application to Irma Category 5 Hurricane

Alexis Mouche[1], Bertrand Chapron[1], John Knaff[2], Yili Zhao[3], Biao Zhang[4], and Clément Combot[1]

[1]IFREMER, Université Brest, CNRS, IRD, Laboratoire d'Océanographie Physique et Spatiale, Brest, France, [2]NOAA/NESDIS Regional and Mesoscale Meteorological Branch, Fort Collins, CO, USA, [3]National Ocean Technology Center, State Ocean Administration, Tianjin, China, [4]School of Marine Sciences, Nanjing University of Information Science and Technology, Nanjing, China

Abstract C-band high-resolution radar (synthetic aperture radar [SAR]) is the only spaceborne instrument able to probe at very high resolution and over all ocean basins the sea surface under extreme weather conditions. When coanalyzed with Stepped Frequency Microwave Radiometer wind estimates, the radar backscatter signals acquired in major hurricanes from Sentinel-1 and Radarsat-2 SAR reveal high sensitivity in the cross-polarized channel for wind speeds up to 75 m/s. The combination of the two copolarized and cross-polarized channels can then be used to derive high-resolution surface wind estimates. The retrieval methods and impacts of intense rainfall are discussed in the context of a Hurricane Irma (2017) case study. On 7 September 2017, Sentinel-1 measurements intercepted Hurricane Irma when it was at category 5 intensity. When compared to Stepped Frequency Microwave Radiometer, SAR-derived wind speeds yield bias and root-mean-square of about 1.5 and 5.0 m/s, respectively. The retrieved wind structure parameters for the outer core are found to be in agreement with the Best-Track and combined satellite- and aircraft-based analyses. SAR measurements uniquely describe the inner core and provide independent measurements of the maximum wind speed and the radius of maximum wind. Near the radius of maximum wind a 65-m/s increase in wind speed in less than 10 km is detected, corresponding to an instantaneous absolute vorticity of order 210 times the Coriolis parameter. Using a parametric Holland model and the environmental surface pressure (1,011 hPa), SAR-derived wind speeds correspond to a central surface pressure of 918 hPa (921 hPa from the Best-Track) in Irma's eye.

Key Points:
- No saturation of the cross-polarized C-band ocean backscattered signal for surface wind speeds up to 75 m/s is observed
- Combined copolarization and cross-polarization are used for ocean surface wind retrieval from Sentinel-1 and Radarsat-2 SAR over major hurricanes
- Irma category 5 hurricane wind structure is described at high resolution O(1 km) and compared with other existing and independent analysis

Correspondence to:
A. Mouche,
alexis.mouche@ifremer.fr

Citation:
Mouche, A., Chapron, B., Knaff, J., Zhao, Y., Zhang, B., & Combot, C. (2019). Copolarized and cross-polarized SAR measurements for high-resolution description of major hurricane wind structures: Application to Irma category 5 hurricane. *Journal of Geophysical Research: Oceans*, *124*, 3905–3922. https://doi.org/10.1029/2019JC015056

Received 14 FEB 2019
Accepted 9 MAY 2019
Accepted article online 15 MAY 2019
Published online 19 JUN 2019

1. Introduction

While a variety of sources for tropical cyclone (TC) wind data is now available (e.g., (Reul et al., 2017), the only routine observations in the high-wind inner core region comes from aircraft reconnaissance, limited to TCs occurring in the North Atlantic and East Pacific. In this context, C-Band high-resolution radar (or SAR for synthetic aperture radar) is the only spaceborne instrument able to probe and uniquely quantify, at very high spatial resolution O(1 km), ocean sea surface information under extreme conditions (Fu & Holt, 1982; Horstmann et al., 2005, 2013; Katsaros et al., 2000; Zhang & Perrie, 2012). Indeed, SAR measurements can be acquired day and night, regardless of the cloud coverage, with pixel resolution of few meters in swaths of several hundred kilometers. In addition, recent SAR missions, with enhanced polarization diversity, have led to new prospects to use radar measurements (cross section, Doppler) to retrieve geophysical parameters (Mouche et al., 2012). In particular, Radarsat-2 capabilities to measure the backscattered signals in copolarization and cross-polarization (antenna emits in Vertical polarization and receives in Horizontal polarization; or vice versa) opened for new analysis strategies (Kudryavtsev et al., 2013, 2014), to help reveal and interpret surface roughness changes related to upper ocean dynamics. For extreme weather events, such as TCs, the expected high sensitivity of cross-polarized signals to ocean wave breaking further translated into a new potential: the use of these new cross-polarized signals to map, at very high resolution, variations in ocean surface winds in and around the TC eyes (Mouche et al., 2017; Zhang & Perrie, 2012). Early demonstrations rapidly triggered vast interests, leading to refinements of future concept missions (Fois et al., 2015) to best exploit this high sensitivity to high wind conditions. In that context, EUMETSAT (European Organization for the Exploitation of Meteorological Satellites) together with ESA (European Space Agency) already

planned to add a cross-polarized channel for the next generation of operational scatterometer mission (i.e., the next Polar System Second Generation) dedicated to the ocean surface wind vector measurements at medium resolution (Stoffelen et al., 2017).

The new European SAR mission, namely, Sentinel-1, also benefits from these polarization diversity. As part of the European Copernicus program, the continuity in data acquisitions will be ensured for the next decade. In the present study, the motivation is thus to further document the benefit of having a cross-polarized channel to characterize and map ocean surface winds in extreme TC weather conditions. As reported below, investigations are performed at high resolution, as available with SAR missions, but results also directly contribute to the next generation of European medium-resolution scatterometers. Moreover, the focus is to further assess the potential of using both Sentinel-1 and Radarsat-2 SAR measurements and more specifically to report on cases corresponding to very intense events, that is, category 3, category 4, and category 5 TCs. Based on Sentinel-1 acquisitions over the major Hurricane Irma (2017), we illustrate how combined C-band dual-polarized SAR measurements can uniquely provide quantitative information on the wind structure in both the inner and outer cores.

For our purpose, the analysis concentrates on specific acquisitions over North Atlantic TCs, to maximize the chance to compare satellite measurements with coincident airborne ones. The goal is first to more precisely document the relationship between the radar cross-polarized cross-section measurements and ocean surface wind speeds during very extreme events, with maximum wind speeds higher than 50 m/s. Cases have thus been selected with respect to their intensity and, more importantly, for the collocation opportunities with airborne measurements from the Stepped Frequency Microwave Radiometer (SFMR) instrument. The SFMR provides independent measures of rain rate and ocean surface wind speed (Klotz & Uhlhorn, 2014; Uhlhorn et al., 2007). Then, we consider particular acquisitions during Irma, one of the strongest North Atlantic TCs recorded during the 2017 season. To recall, most previous studies hardly sampled wind speed conditions higher than 40 m/s (Hwang et al., 2015) or 50 m/s (Mouche et al., 2017). Section 2 presents the data sets we used and the collocation method we applied. Section 3 focuses on the relationship between the normalized radar cross section (NRCS) and the wind speed as given by SFMR measurements. Section 4 is the Irma case study, detailing the wind field obtained from SAR and discussing the results with respect to independent analysis.

2. Data Set

2.1. Sentinel-1 and Radarsat-2 C-Band SAR

Sentinel-1 mission is part of the European and operational Copernicus program space component. This is a constellation of two satellites (S-1A and S-1B units). Both Sentinel-1A and Sentinel-1B carry a C-band SAR and provide continuity with previous European (ERS-1 and ERS-2) and ENVISAT missions. Sentinel-1A and Sentinel-1B were launched in April 2014 and 2016, respectively. They have four exclusive imaging modes: Interferometric Wide swath (IW), Extra Wide (EW) swath, Strip Map (SM), and Wave (WV) modes. This study solely concentrates on IW mode. The IW swath is 250 km wide and covers incidence angles from about 30° to 46°. When processed into Level-1 (L1) GRDH (Ground Range Detected High resolution), IW Sentinel-1 products have a resolution of about 20 m in range (across track) and 22 m in azimuth (along track). C-band Radarsat-2 SAR was launched in 2007 and is the first SAR able to provide dual-polarized (and quad-polarized) images (VV+VH or HH+HV) with different acquisition modes including different resolutions and swath dimensions. In this study, we rely on Radarsat-2 SCANSAR Wide (SCW) imaging mode, with incidence angles ranging from 20° to 49 ° and a resolution of about 100 m in both range and azimuth directions. These two RS-2 SCW and S1 IW wide swath modes allow acquisitions in dual polarization, two images being acquired over the same area at the same time. One is in copolarization (VV or HH), and the other is in cross polarization (VH or HV). In this study we only use L1 data acquired in dual polarization (VV+VH) to take benefit of the two polarization channels for the SAR wind retrieval (Mouche et al., 2017). To note, the EW Sentinel-1 acquisition mode has also the dual-polarization capability with a larger swath (400 km wide) more adapted to hurricane monitoring. Moreover, CSA (Canadian Space Agency) will launch in 2019 the Radarsat-2 mission follow-on (Radar Constellation Mission), and ESA already planned Sentinel-1C and Sentinel-1D to ensure continuity up to 2030.

At C-band over the ocean, the NRCS acquired in cross polarization is typically 10 to 100 times lower than in copolarization, depending on radar incidence angle and geophysical conditions. The NRCS accuracy and the signal-to-noise ratio are thus the main limitations for applications based on cross-polarized signals. The

potential of Sentinel-1 dual-polarized acquisitions for ocean applications (Mouche & Chapron, 2015) and a first algorithm for ocean surface wind measurements over extremes (Mouche et al., 2017) have already been presented. Sentinel-1 mission requirements for radiometric accuracy is 1 dB. According to measurements acquired over DLR (Deutsches Zentrum fr Luft- und Raumfahrt) transponders, the relative radar cross section for IW modes has been evaluated in 2017 at -0.06 ± 0.16 dB for Sentinel-1B and at -0.1 ± 0.15 dB for Sentinel-1A. Sentinel-1 IW and Radarsat-2 SCW Level-1 data analysis give noise equivalent sigma zero (NESZ) values between -30 and -23 dB depending on elevation angle. The NESZ is different for each subswath and further range dependent (i.e., modulated across the subswaths) inside each subswath (see Figure 2 in Mouche & Chapron, 2015). For Sentinel-1, since this preliminary assessment, ESA has already improved the NESZ estimates with respect to range direction but also azimuth direction in order to mitigate subswath jumps and azimuth scalloping (Miranda et al., 2017). The Level-1 processor has been recently revised accordingly (IPF V2.90) to annotate more accurate NESZ in the product. A technical note on the annotated noise in Sentinel-1 Level-1 products has been published and details all stages to properly correct the NRCS from noise (Piantanida et al., 2017). In this study, we strictly rely on Sentinel-1 products reprocessed with IPF V2.90 to take into account the latest and most accurate annotated noise available, and we apply the technical note methodology.

2.2. Hurricane Tracks

Best-Tracks are post-storm analyses of the intensity, central pressure, position, and size of tropical and subtropical cyclones. They are produced by Regional Specialized Meteorology Center or Tropical Cyclone Warning Center (RSMC and TCWC) after the hurricane season and include all available data from buoys, platforms, and surface and satellite (no SAR) observations to provide TC parameters at each synoptic hour (00, 06, 12, and 18 hr). Additional information such as wind radii or time and intensity of landfall can also be provided by RSMC and TCWC. Given the different ocean basins, the variety of involved agencies, and the nonhomogeneity of the different sources, building a homogeneous (format and quality) and global database is not straightforward (Kruk et al., 2010). This is the main purpose of the IBTraCS database (Knapp et al., 2010). This data set gathers all available Best-Tracks for all storms and all basins and follows the World Meteorological Organization (WMO) recommendations. In this study, we use the IBTraCS database because it provides storm intensities and the wind structure parameters such as wind radii (64, 50, and 34 knots), or maximum sustained wind radius. To note, in case of unavailability of these Best-Tracks (as they are produced several months after the hurricane season), one can rely on the Automated Tropical Cyclone Forecasting System proposed by Sampson and Schrader (2000). Indeed, this system, fed by National Hurricane Center (NHC; for east Pacific and north Atlantic basins) and Joint Typhoon Warning Center (JTWC; for the others), was designed to optimize forecasting processes and warning messages issues and to maintain a tracks archive for past and active storms (Miller et al., 1990). These "operational Best-Tracks" are produced in near-real time and are reanalyzed after the season to feed the HURDAT database (Rappaport et al., 2009). Although some of the parameters can suffer from large errors (e.g., >25% for radius of maximum wind speed (Landsea & Franklin, 2013; Schreck et al., 2014) or discrepancies between different agencies (mostly in Western Pacific basin as shown by Knapp et al., 2010; Sampson et al., 2018), Best-Tracks remain a valuable source of information regarding the evolution of a TC during its whole lifetime (Knapp et al., 2010). In this study, because SAR observations are not used to produce hurricane tracks (including reanalysis of Best-Tracks), they are used as independent measurements for comparison.

2.3. Combined Satellite Aircraft Analysis

In this study, a combined satellite aircraft analysis is used for comparisons with SAR-based wind retrievals. This analysis combines the multisatellite platform TC surface wind analysis (Knaff et al., 2011) with aircraft reconnaissance data collected from the real-time high-density observations distributed via the global telecommunication system. Reconnaissance data contain flight-level wind, temperature dew point, and altitude information and surface wind speed estimates from SFMR. The aircraft collect data over several hours, and for most of the sorties sample in an α-shaped pattern (see Figure 1); making multiple passes through the center of circulation.

The temporal composite of data occurs over a 6-hr time window, and the final analyses are centered at the synoptic times. To perform the data composite, cubic splines are used to estimate the position of the storm at the time of the observation from which a radius and azimuth is calculated following the storm. Storm positions come from a combination of the operational best track (before and after the aircraft sortie) and the routine aircraft-based center fixes (during the time the aircraft is sampling the storm).

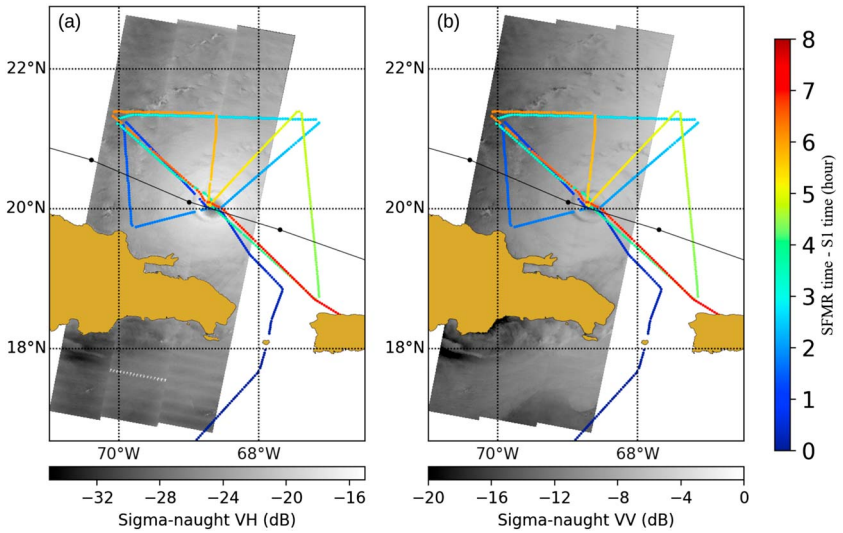

Figure 1. Maps of normalized radar cross section (NRCS) as measured by Sentinel-1A over Irma category 5 hurricane on 7 September 2017. (a) NRCS in VH polarization. (b) NRCS in VV polarization. The locations of SFMR measurements after collocation are overlaid with color code indicating SFMR-derived ocean surface wind speed. SFMR = Stepped Frequency Microwave Radiometer.

The variational data-fitting methodology of the analysis follows that described in Knaff et al. (2015) where flight-level (700 hPa) wind vectors and SFMR wind speeds (corrected to flight level) are analyzed on a polar grid with radial resolution of 2 km and azimuthal resolutions of 10°. The enhancements of wind speeds to flight level and the reductions of the final analysis to a 10-m marine exposure follow recommendations in Franklin et al. (2003). The two ways these analyses differ from those used in Knaff et al. (2015) are that the satellite-only analyses are used as initial wind estimate or first guess and that a residual analysis is performed. The residuals are analyzed using the same variational methodology with smaller azimuthal and radial data filters. When the residuals are added back into the analysis, the resulting winds are closer to the observations as the fine-scale residual analysis acts much like multiple passes through a Barnes (1964) analysis as demonstrated in Koch et al. (1983). Following the final analysis and residual correction, winds are reduced to a 10-m marine exposure and inflow angles applied as suggested in Zhang and Uhlhorn (2012). If a point is actually determined to be over land, winds are reduced an additional 20% and the inflow angle is increased an additional 20°. These winds were then interpolated to a $0.05° \times 0.05°$ Cartesian grid.

The resulting analysis produces a spatially continuous data set that closely fits the input data, objectively replicating what a detailed subjective analysis of the data would produce. It is noteworthy that the variational analysis tends to more heavily weight flight-level vector wind components compared to the scalar SFMR wind speeds because (1) wind speed is the scalar magnitude of the wind vector and (2) the cost function minimizes the sum of errors in tangential vectors, radial vectors, and wind speeds. Thus, the resulting analysis is fundamentally different than one produced using SFMR wind speeds alone. We will refer to this as the Multi-observation Tropical Cyclone Surface Wind analysis (MTCSWA), hereafter.

2.4. Next-Generation Radar

NEXRAD (for Next-Generation Radar) is a network of 160 high-resolution Doppler weather radars operated by the National Oceanic and Atmospheric Administration (NOAA) National Weather Service, the Federal Aviation Administration, and the U.S. Air Force (USAF). They are located in the contiguous United States, Alaska, Hawaii, U.S. territories, and at military base sites. Thirty-four stations out of the 160 stations are located in coastal areas. NEXRAD Level-II and Level-III products are routinely available from the NOAA National Centers for Environmental Information. Level-II products provide the three meteorological base data quantities: reflectivity, mean radial velocity, and spectrum width, while there are over 75 different Level-III products such as storm relative velocity, vertical integrated liquid, or 1-hr precipitation (Federal Meteorological Handbook No. 11—Doppler Radar meteorological observations (WSR-88D). Part C: WSR-88D products and algorithms, 2017). In this study, we only consider Level-III products of base reflectivity. The radar scan time is 4.5 min, and the resolution is 1 km in range direction and 1° in azimuth with a

radius coverage of about 450 km. Note that the 1-hr precipitation product has been discarded as it is much less correlated with SAR signal due to the large (60 min) integration time.

2.5. Stepped Frequency Microwave Radiometer

Each Atlantic and East Pacific hurricane season, the Hurricane Research Division conducts a field program in which they collect data with the NOAA and, since 2007, the USAF aircrafts. Airplanes fly directly into the eye of the hurricane, usually adopting an "alpha" or "multi-alpha" pattern (see Figure 1), to best sample the four geographical quadrants. They carry SFMR, a stepped frequency microwave radiometer providing wind speed and rain rate estimates. Initially operated in 1980, SFMR measurements are now routinely acquired by NOAA and USAF aircrafts and operationally processed to be transmitted to the NHC (in Miami and Honolulu). The wind estimate principle relies on the use of six different C-band frequencies between 4.5 and 7.2 GHz to correct for rain-induced effects. SFMR measurements' temporal resolution is 1 s. The validation of retrieved wind speeds against Global Positioning System (GPS) dropwindsondes using 3 years of data by Uhlhorn and Black (2003) for a range of wind speeds from 10 to 60 m/s yields to a root-mean-square error of 3.3 m/s and indicates a possible bias due to ocean surface waves. SFMR processing algorithm has been further revised by Uhlhorn et al. (2007) to extend the range of wind speed up to 70 m/s and remove a remaining bias for moderate SFMR-measured wind speeds (10–50 m/s). Because the SFMR design involved a single nadir-viewing antenna, the data only provide transects of the wind speeds and not the full two-dimensional wind-speed pattern of the hurricane system. However, the combined estimates of rain rate and ocean surface wind speed makes this instrument unique for SAR wind speed validation and to discuss the possible rain impact on SAR measurements.

2.6. SAR Data Collection

To date, SAR missions cannot continuously acquire wide swath data in high-bit rate modes. As a consequence, tasking SAR with respect to the hurricane tracks forecast is required to jointly maximize acquisitions over TCs and mitigate the impact on the whole acquisition plan. This implies solving potential conflicts between users regarding the duty cycle along the orbit and the acquisition modes to be used over a given area of interest. Since 2016, ESA organizes specific S-1 acquisition campaigns to test the instrument capabilities for mapping, at very high resolution, extreme (TC) ocean wind conditions. These campaigns of dedicated acquisitions are named as SHOC, for Satellite Hurricane Observations Campaign (Mouche et al., 2017). Fully coordinated as for the hurricane watch program approach (Banal et al., 2007), SHOC campaigns help maximize the number of SAR acquisitions for both Copernicus/ESA Sentinel-1 and also MDA/CSA Radarsat-2 missions. For this study, the strategy to collect the data includes two different approaches. (i) As part of SHOC, we collect the data through acquisitions requests for both Radarsat-2 and Sentinel-1 missions, respectively, to MDA and ESA. These requests were based on 5-day forecasts of the hurricane track and satellite orbit. This approach requires great flexibility for the data provider. (2) We also analyze the SAR data archives and the maximum wind speed with respect to the hurricane Best-Tracks database. The period considered for the archive analysis is from 2015 and 2017. We only applied the second method to the Rasarsat-2 data. Indeed, SHOC provided all dual-polarized acquisitions over TC since the beginning of Sentinel-1 mission. Then, as a final and common step, we apply two additional criteria to consider only SAR data acquired (1) over hurricane eyes when maximum wind speeds are larger than (or equal to) 50 m/s and (2) with airborne data available.

In total, the SHOC campaign provided six SAR observations corresponding to four different TCs in 2015–2017. The list of the SAR observations, associated TC name, and intensity category during the observations are given in table 1. Three have been acquired during category 5 intensity, one during category 4 TC intensity, and three during category 3 intensity. An example of SAR acquisition and the collocated SFMR measurements locations is shown for Sentinel-1 data acquired in VH (Figure 1a) and VV (Figure 1b) polarizations over Irma TC, on 7 September 2017. In Figure 1, SFMR measurements locations are indicated by colored dots, and the color code indicates the time difference between SAR acquisition and SFMR measurements. In this case, up to five transects across the eye have been performed for a flight lasting about 8 hr.

3. Data Analysis

3.1. Collocation

The collocation of rain and ocean surface wind speed measurements involves several steps. First, SFMR measurements are smoothed using an averaging moving window of 10 s and a spatial resampling at 3 km. During

Table 1
SAR Acquisitions and Corresponding Hurricane Information

Sensor	Acquisition mode	Polarization	SAR observation starting date UTC	SAR observation ending date UTC	TC Name	TC category before/after	Collocated SFMR
Radarsat-2	ScanSAR Wide	VV, VH	2015/10/03 10:44:58	2015/10/03 10:45:12	Joaquin	4/4	1
Radarsat-2	ScanSAR Wide	VV, VH	2016/09/02 03:53:04	2016/09/02 03:53:17	Lester	3/3	1
Sentinel-1A	Interfero-metric Wide	VV, VH	2017/09/07 10:29:51	2017/09/07 10:31:10	Irma	5/5	1
Radarsat-2	ScanSAR Wide	VV, VH	2017/09/08 10:53:52	2017/09/08 10:54:04	Irma	5/4	2
Radarsat-2	ScanSAR Wide	VV, VH	2017/09/18 22:07:22	2017/09/18 22:07:36	Maria	3/5	1
Radarsat-2	ScanSAR Wide	VV, VH	2017/09/22 10:45:38	2017/09/22 10:45:51	Maria	3/3	1

Note. Dates are formatted as year/month/day.

this preprocessing step, the quality flag included in SFMR data can be used to possibly filter out low-quality data. Second, the hurricane translation speed is computed from the hurricane track. The locations of SFMR measurements are then shifted with respect to the time difference between each SFMR measurements and the SAR acquisition time using the TC motion vector. The duration of a SAR acquisition is typically few seconds (see the fourth and fifth columns in Table 1), whereas a flight with SFMR can last up to 6 hr and more. SAR time is thus considered constant with respect to SFMR times. Starting acquisition time is used for SAR acquisition time. If several acquisitions performed in a row are necessary to describe the whole hurricane, the duration of SAR acquisitions increases. For instance, in the case of Irma presented in Figure 1, a total of four successive acquisitions are concatenated to produce the image, leading to an acquisition duration of 1 min and 29 s. Finally, for each SFMR storm-motion-relative location, oceanic SAR measurements are averaged within a radius R. Note that this step results in a collocated SAR data set with a pixel spacing of 3 km but a spatial resolution depending on R. In this study we used R =1.5, 2.5, 6, 12.5, and 25 km to mimic different spatial resolutions.

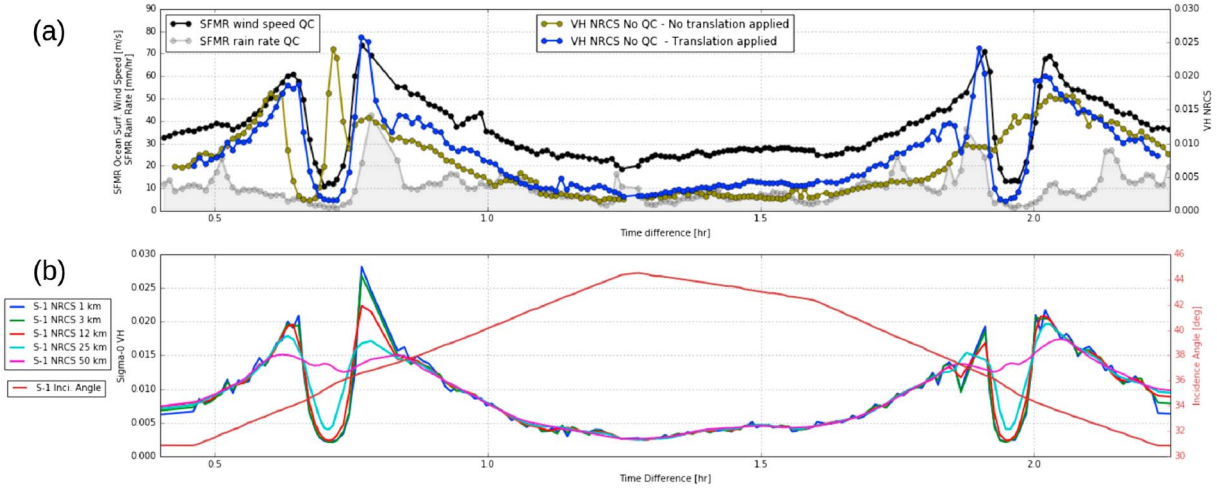

Figure 2. Transect of collocated SFMR and SAR measurements at 3-km resolution. (a) Quality-controlled SFMR ocean surface wind speed (black) and rain rate (gray). NRCS in VH polarization with (blue) and without (olive) taking into account Irma translation speed during the collocation. (b) Same Sentinel-1A NRCS transect as in (a) but for different resolutions (1, 3, 12.5, 25, and 50 km). Variation of SAR incidence angle along the transect is indicated in brown (right y axis). SFMR = Stepped Frequency Microwave Radiometer; SAR = synthetic aperture radar; NRCS = normalized radar cross section; QC = quality controlled

An example of collocation obtained for Irma between Sentinel-1A and SFMR is given in Figure 2. Figure 2a shows the SFMR ocean surface wind speed and rain rate estimates as a function of time. Here the quality flag included in the SFMR data has been taken into account. *X* axis indicates the time difference with respect to SAR acquisition time. In the present study, we only focused on collocations with an absolute time differences less than 2.5 hr. In this case, measurements up to 75 m/s have been measured by SFMR. These large values of wind speed strongly correlated with the highest values of rain rate, corresponding the western part of the TC eye, very close to the radius of maximum wind (RMW). The nonflagged observations appear to contain wind estimates where rain rates, which are discussed later, are up to 40 mm/hr. To note, flagged measurements reach rain rates up to 80 mm/hr (see Figure 8). This suggests that the quality procedure removes measurements for the most intense rain rates. Figure 2a also presents the collocated cross-polarized NRCS (blue) with respect to time corresponding to the same SFMR measurements. As observed and already reported with SAR data from Radarsat-2 mission, there is a very strong correlation between SFMR ocean surface wind speeds and cross-polarized NRCS at C-Band (Zhang & Perrie, 2012). Figure 2a also shows the match-ups that result if the collocation procedure is not performed. The olive line shows NRCS that has not been aligned with TC motion. In this case the strong correlation between SAR and SFMR measurements is completely lost.

The impact of the different spatial resolutions is presented in Figure 2b. This comparison shows the benefit of high-resolution compared to medium-resolution missions such as L-band radiometers (about 40 km for Soil Moisture Active Passive (SMAP); Meissner et al., 2017; Yueh et al., 2016; or Soil Moisture and Ocean Salinity (SMOS); Reul et al., 2012) or scatterometers (about 25 km for nominal resolution with the next European SCA on MeTop SG; Stoffelen et al., 2017). In this case, larger averaging areas blur the interpretation of the data, clearly showing that both the central wind minimum and peakedness of the wind maxima are severely impacted at spatial resolutions exceeding 12 km. In fact, at the time of acquisition, Irma eye diameter was about 30 km (about 16 nautical miles) as given by the Best-Track analysis, corresponding to less than three measurements at 25-km resolution. When the pixel sampling decreases, results are even worse (not shown). More generally, the use of SAR acquisitions with NRCS computed at different resolutions to systematically mimic lower resolution sensors can certainly help to characterize the resolution impact on the measurements depending on TC characteristics, particularly in the high wind-speed gradient areas near the RMW.

3.2. Radar Backscattering Versus SFMR Measurements

Using a 3-km resolution, all collocated measurements between SAR and quality-controlled SFMR measurements can now be used to more precisely document the relationship between cross-polarized NRCS and ocean surface wind speeds, including local extremes up to 80 m/s. For this purpose, Sentinel-1 and Radarsat-2 data are combined.

As explained in section 2, and especially for weak cross-polarized backscattered signals, the signal-to-noise ratio is a key measurement, highly dependent upon the accuracy of the noise annotated in the SAR products. To note, noise corrections were often neglected (Zhang & Perrie, 2012) or not always properly taken into account for the entire data set (Hwang et al., 2015). Here, all SAR data are noise-corrected before collocation.

The impact of the noise correction on the NRCS relationship with ocean surface wind speed is illustrated in Figure 3a without noise correction and in Figure 3b with noise correction. Both cases show that the NRCS clearly increases with ocean surface wind speed, without any apparent NRCS saturation in wind speeds up to 75 m/s. With or without noise correction, these comparisons confirm the substantial potential of C-Band cross-polarized NRCS for retrieving oceanic surface wind speeds in TC environments over TCs, including category 4 and category 5 hurricanes. Nonetheless, NRCS to wind relationships, obtained with and without noise correction, are impacted by noise over the whole range of wind speeds. As anticipated, this impact can become particularly significant for the lowest branch of the high wind speed range (wind speed $\simeq$20m/s). Without noise correction, our present analysis consistently recovers previously reported relationships (or GMF, for geophysical model function) between NRCS and wind speeds, especially those developed for wind speeds lower than 30 m/s (Zhang & Perrie, 2012; Zhang et al., 2017). The application of noise correction fully explains the difference observed between our analysis and reported GMFs in this range of wind speeds. For higher than 30 m/s wind speeds, these GMFs are not adapted and simply fail to explain the collected data. The present analysis demonstrates that noise-corrected NRCS values increase from about −36 dB at 5 m/s up to −16 dB at 70 m/s. This analysis also reveals, for the first time, the great consistency of the two

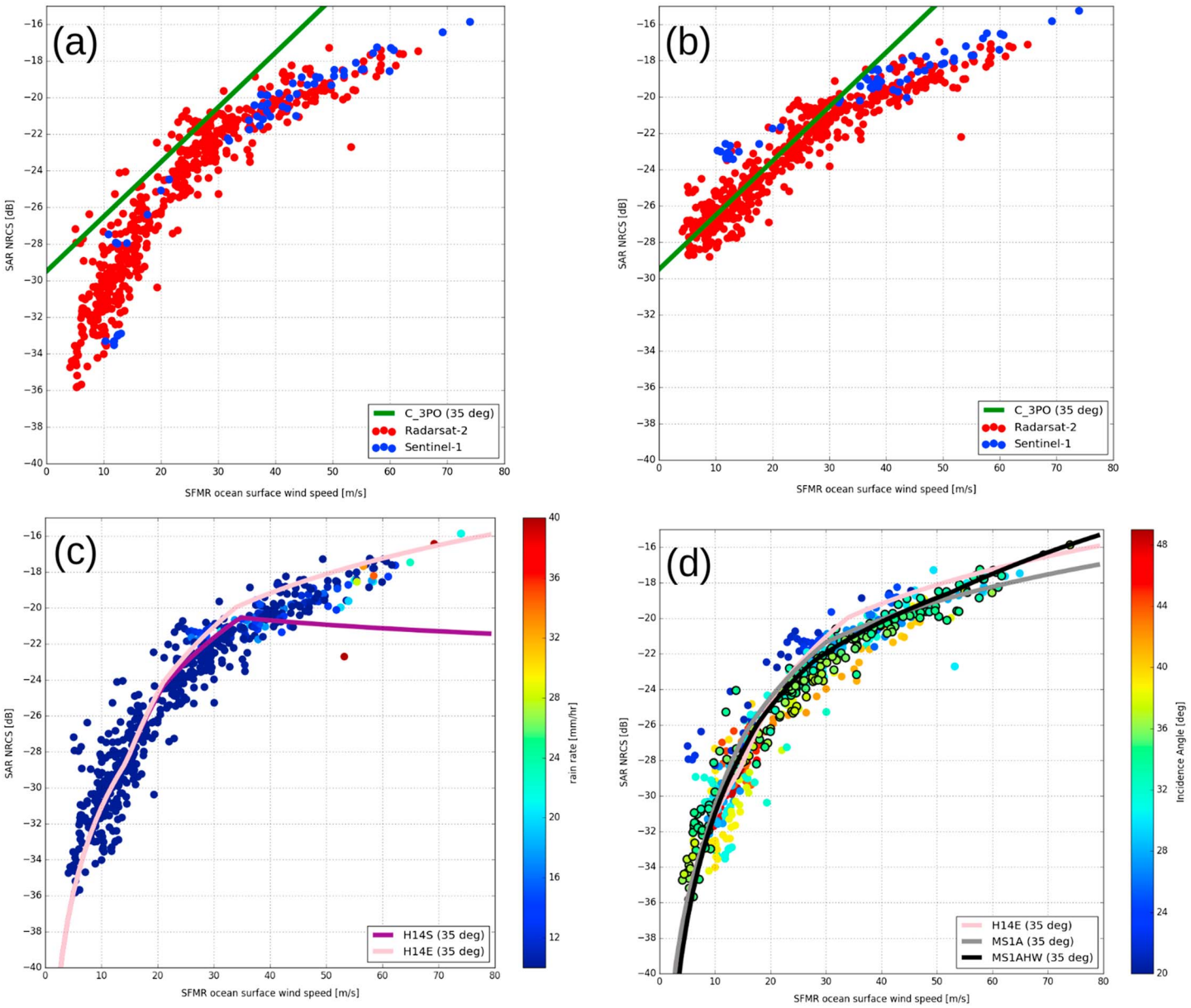

Figure 3. Three-kilometer Sentinel-1A (blue) and Radarsat-2 (red) NRCS in VH polarization (a) with noise correction and (b) without noise correction, and as a function of the ocean surface wind speed measured by SFMR. Green solid line stands for the GMF proposed by Zhang et al. (2017). (c) Same as (a) but with color code indicating SFMR rain rate. Pink and purple solid lines respectively indicate H14E and H14S GMF from Hwang et al. (2015). (d) Same as (a) but with color code indicating SAR incidence angle. Pink and gray solid lines respectively indicate H14E GMF from Hwang et al. (2015) and MS1A GMF from Mouche et al. (2017). NRCS = normalized radar cross section; SFMR = Stepped Frequency Microwave Radiometer; GMF = geophysical model function; SAR = synthetic aperture radar.

different SAR missions (RS2 and S-1), regarding their calibration. This clearly demonstrates the potential to systematically combine the different instrument measurements in order to increase the temporal sampling of a given storm. In the following, we only consider NRCS corrected for noise annotated in the product.

Comparisons with other existing GMFs are presented in Figure 3c. The two GMFs proposed by (Hwang et al., 2015) display significantly different behaviors for wind speeds higher than 35 m/s—note the relative saturation in the H14S GMF. The present analysis reveals that, between 35 and 70 m/s, H14E GMF is clearly more adapted than H14S GMF. For this figure, the rain rate measured by SFMR is also reported. In our analysis, data show no evidence of significant degradation due to the presence of precipitation. For wind speeds between 5 and 30 m/s, the rain rate is lower than 20 mm/hr, and its effect on NRCS computed at 3 km

is hardly visible. Few measurements with rain rate between 20 and 40 mm/hr and wind speeds larger than 30 m/s have been collected, and in those cases, precipitation impacts are unclear. It is however noteworthy that around 52.5 m/s wind speed, an outlier in NRCS is obtained for 40 mm/hr rain rate. This latter result tends to indicate possible significant decreases of NRCS for high rain rates. The impact of rain rates on NRCS and retrievals is further discussed in section 3.3 based on a detailed case study.

In Figure 3d colors provide the SAR incidence angles. Overall, NRCS measurements decrease when the incidence angle increases. Here, this decrease can be observed up to 50 m/s. This result agrees with previous studies (Hwang et al., 2015; Mouche et al., 2017; Zhang et al., 2017). The lack of cases at higher wind speeds prevents any conclusion of the impact of incident angle on NRCS at those speeds. Future studies that make use of larger numbers of cases will be used to address this issue. Results of H14 E GMF from Hwang et al. (2015) and MS1A GMF from Mouche et al. (2017) are reported at 35° incidence angle and are also shown in Figure 3. For comparison, circles surrounded with black lines indicate measurements with incidence angle between 32.5° and 37.5°. Both GMFs agree quite well with the data. At wind speeds above 30 m/s, differences appear, with an overestimation of the NRCS for H14E GMF between 30 and 60 m/s, and an underestimation of the NRCS for MS1A GMF for wind speeds larger than 50 m/s. This is not surprising. The H14E GMF has been derived with wind speed measurements up to 40 m/s, while MS1A GMF definition relies on medium resolution wind speed from SMAP L-Band radiometer up to 50 m/s. Based on these new collected data, we have slightly modified MS1A, to fit the observations up to 70 m/s. We will refer to this new formulation as MS1AHW throughout.

3.3. Applications and Discussions

Hereafter, a case study is detailed. The case corresponds to Sentinel-1 measurements acquired over Hurricane Irma, as already presented in the previous sections. Following the approach from Mouche et al. (2017), an algorithm, jointly using copolarized and cross-polarized SAR signals, is applied to estimate ocean surface wind speeds using the MS1AHW GMF. Because concurrent high-resolution surface information does not exist, it is not straightforward to validate the resulting 2-D structure of SAR ocean surface wind speeds. As a first step, we directly compare SAR and SFMR wind speeds along aircraft translation segments. In addition, the overall TC structure derived from the SAR analysis can be compared to the MTCSWA.

Comparisons are also performed with standard operational TC parameters used to describe the hurricane wind structure at Regional Specialized Meteorological Centers. Particular attention is given to the wind radii in the four geographical quadrants NE, NW, SW, and SE provided by the Best-Track analysis. To recall, operational techniques subjectively combine a variety of sensors, including radiometer- and scatterometer-based measurements. In comparison with these other observations of chance, SAR systems provide very high resolution ocean surface information, largely interpreted in terms of wind intensity and structure. SAR wind speed estimates can provide similar structural estimates as aircraft reconnaissance, but observations nearly instantaneously made over the whole inner core area of the TC.

3.3.1. Ocean Surface Wind Structure

When hurricane Irma was observed by Sentinel-1 SAR, on 7 September 2017, it had category 5 intensity according to National Hurricane Center report (Cangialosi et al., 2018) and Best-Track analysis. The wind speed map, as derived from SAR along the SFMR transects, is presented in Figure 4a, where the quality-controlled wind speed measurements from SFMR are also superimposed using the same color code. An overall agreement is clearly obtained between Sentinel-1 and SFMR wind speeds. Two rings of maximum wind speeds are noticeable, around the eye at radii of about 20 km (≈ 10 n.mi) and 30–35 km (≈ 15-20 n.mi). For the highest values of wind speed, the agreement is even more remarkable (see Figure 4c). This is essentially the result of using the cross-polarization information in the retrieval scheme (Mouche et al., 2017). Note that SAR's high resolution captures the full dynamic range of the wind speed gradient in the eyewall, where wind speeds vary from 10 to 80 m/s in less than 20 km (≈ 10 n.mi). A scatter plot of SAR wind speed estimates versus SFMR ones is presented in Figure 4b. Blue dots indicate data collocated within 3 hr, whereas red dots are collocated data without any criteria time criterion. The overall bias is 1.41 m/s, with a standard deviation of 5.14 m/s, a correlation coefficient of 94%. As expected, such a performance largely degrades as the collocation time difference increases, especially for this intense TC. The time difference becomes more crucial than in other typical studies where wind gradients are smoother or satellite-derived winds are retrieved at coarser resolution. As an illustration of the collocation limitations, a slight misalignment between Sentinel-1 NRCS and SMFR ocean surface wind speeds can be observed in Figure 4c. It is even more obvious during the second transect across the hurricane eye, for which the time difference is about 2

hr. The misalignment is, to first order, likely due to the accuracy of the translation speed, which is based on the 6-hourly and purposely smooth best track. In addition, simply applying a translation, the rotation of the system is also neglected in our collocation method. Nevertheless, these comparisons already provide very encouraging results.

Figure 5 presents the 2-D ocean surface wind speed (a) derived from Sentinel-1 using the dual-polarization approach, (b) MTCSWA, and (c) wind radii-based wind structure provided in the Best-Track. The same color code is used and is defined to indicate the extent of areas corresponding to specific values of 34, 50, and 64 knots that are used by operational services. To ease the visual comparison, the whole Sentinel-1 image is relocated to the storm center location (derived from the MTCSWA product). The original SAR swath limit is also indicated by the black rectangle. The analysis date is 7 August 2017 at 12 UTC for the surface wind analysis and Best-Track products. From Sentinel-1 wind and MTCSWA, we derive the mean ocean surface wind speed profile versus the distance to the TC Eye center, combining data from all geographical quadrants (see Figure 6b), and for each of them (NW, SW, SE, and NE, respectively, in Figures 6c–6f). Wind profiles are indicated in knots to match the units used in operational hurricane centers. We also compute the standard deviation from SAR measurements to highlight the spatial variability at a given radius. The number of SAR measurements used to evaluate this variability as a function of the distance from the TC eye center, is indicated (see *y* axis on right hand side). As expected, the number of SAR data increases with the distance to the TC eye center. Note that over land or for SAR measurements considered of poor quality, data are removed. Finally, Figures 7b–7f also indicate the 34-, 50-, and 64-knot wind radii and the maximum wind speed from Best-Track analysis before (>) and after (<) SAR acquisition time. In spite of the evident differences between the two approaches used to derived the ocean surface wind fields, the two TC structures are in very good agreement. More precisely, the shape of the mean wind profile, the increase of the wind speed in the TC inner core, the RMW, the maximum wind speed value, but also the decay of the wind speed in the outer part of the TC, all these parameters aligned very consistently for both approaches (see Figure 1b). To further note, averaged wind radii are also very close to Best-Track analysis.

Yet, such an overall excellent agreement is not obtained for all quadrants. As a matter of fact, because of the swath coverage and/or land, SAR cannot always equally cover the four geographical quadrants. In this particular case, we observe that the SE, NE, and SW quadrants are less favorable for reliable estimate of the wind radii. The SE and NE quadrants mainly suffer from swath coverage limitations, whereas the SW quadrant is affected by land for a radius between 100 and 300 km. In addition, the aircraft does not cover the whole region where 34- and 50-knot winds are occurring. Moreover, the combined satellite aircraft analysis is likely weighted to the satellite-based first guess. These may explain small discrepancies for 50-knot wind radii. In spite of this limitation, 34-knot wind radii from MTCSWA and SAR still match very well, as more points are usable far from the TC. As computed, derived estimates provide lower values in comparison to Best-Track analysis. Regarding the 64-knot wind radii, the agreement between the three products is clearly satisfying. For the eyewall, a nice match between the two products is obtained, except in the NW quadrant.

The shape of the wind speed profiles in the inner core derived from MTCSWA and SAR are strongly dependent on the precise hurricane center location. As indicated in Figure 6a, they are not the same for the two products. In MTCSWA product, this location appears to be less certain, to possibly explain this difference. Finally, the most significant discrepancies are obtained for radius values between the maximum of backscattered signal and the 64 knots. This is noteworthy for the maximum wind speed and associated radius derived from the wind profile in the NW and SW quadrants. Sentinel-1 wind profiles presented in Figures 6c and 6d indicate sudden changes, with decrease and increase signals between 20 (about 10 n.mi.) and 30 km (about 15 n.mi.). This is not captured in MTCSWA and is directly related to NRCS variations. The combined satellite aircraft analysis is weighted toward flight-level wind vectors, and flight level measurements do not get these variations. Also, the sampling of the aircraft data is every 30 s or $\approx$ 2 km and the analysis has radial smoothing filters with a half-wavelength of 24 km that can prevent fully capturing such kind of short-scale variations in the wind field. As observed on SAR images around the TC eye, NRCS forms a quite distinct darker ring. It is hypothesized that this feature corresponds to localized heavy rain conditions.

For intense TCs, the region of maximum convective rainfall is typically several kilometers outside the RMWs (Jorgensen, 1984). The high NRCS values, adjacent to the dark ring in the SW and NW quadrants, then explain the retrieved very high wind speeds at 20 km (about 10 n.mi.) from the TC center, observed in Figure 4a and in the NW and SW quadrants in Figures 6c and 6d. This is further discussed in the next section.

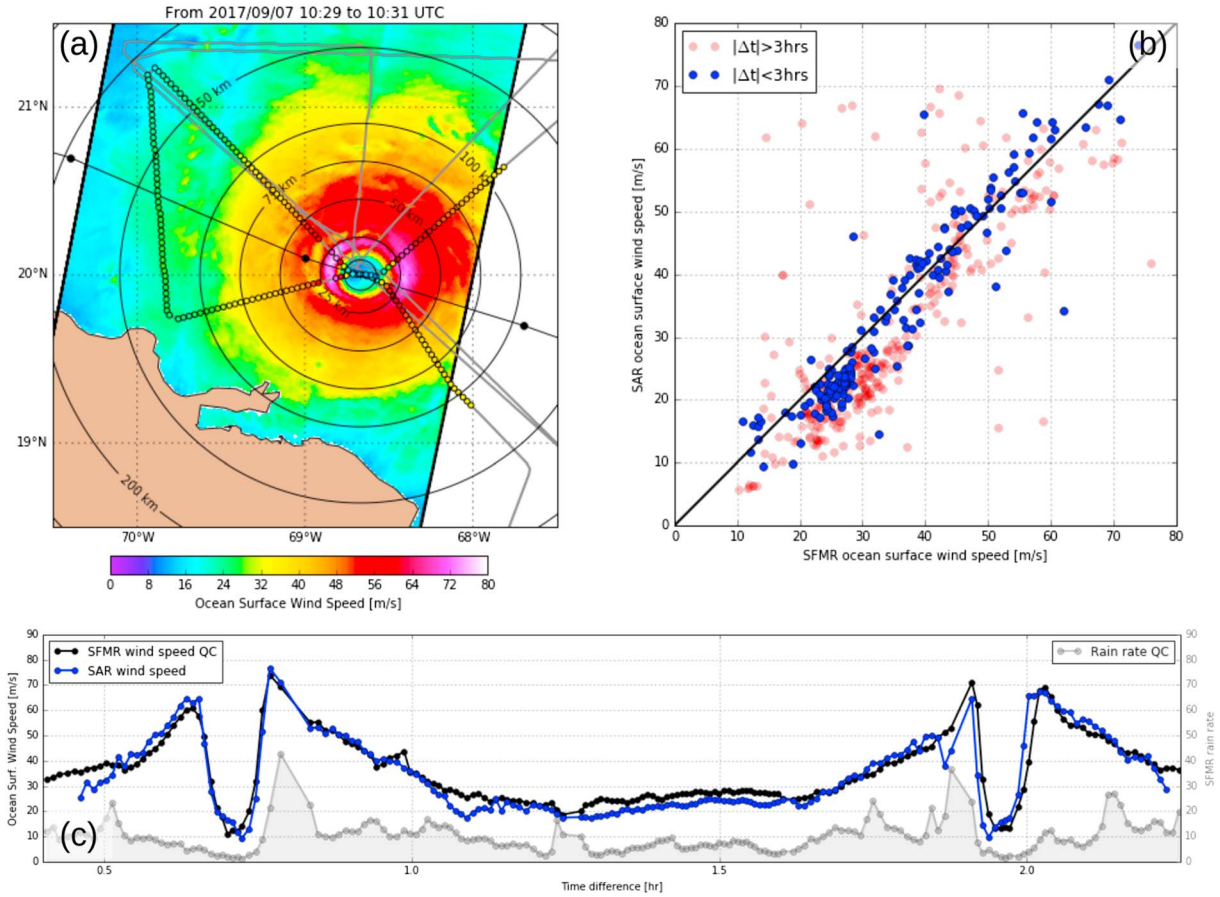

Figure 4. Ocean surface wind speed for Irma category 5 hurricane on 7 September 2017. (a) Map of SAR-derived wind speed. Gray solid line stands for collocated SFMR track. Colored circles along this track indicate SFMR measurements with time difference lower than 2 hr and 30 min. Color code is the same for SAR and SFMR wind speeds. Concentric circles indicate radius from the cyclone center, and dotted black line stands for the Best-Track trajectory, black circle being hurricane position every 6 hr. (b) Scatter plot between SAR-derived and SFMR-derived ocean surface wind speed. (c) Same as Figure 1 but for 3-km resolution ocean surface wind speed from SFMR and Sentinel-1. SAR = synthetic aperture radar; SFMR = Stepped Frequency Microwave Radiometer.

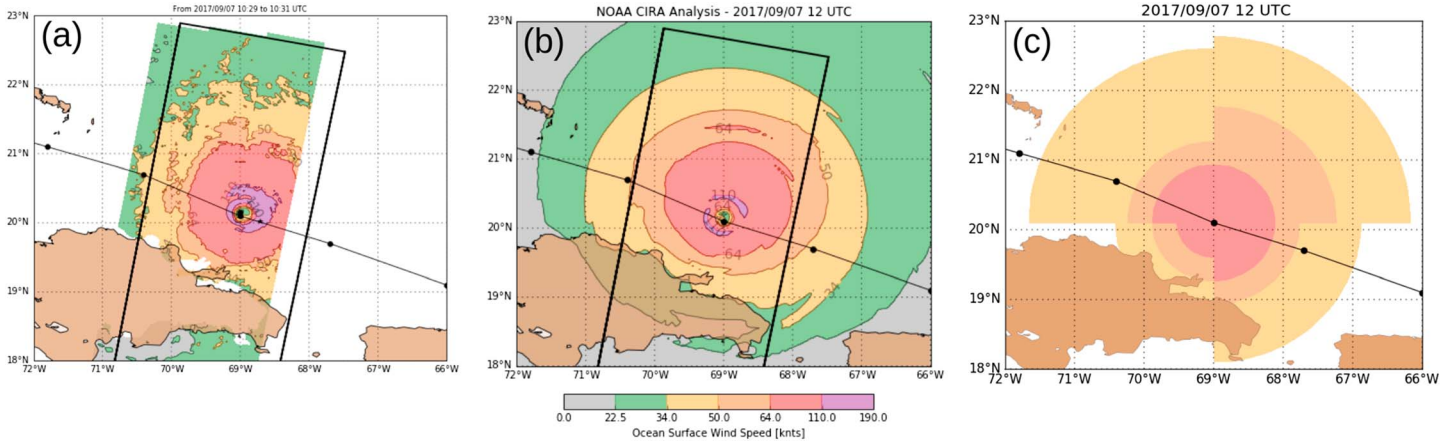

Figure 5. Irma two-dimensional wind structure on 7 September 2017 obtained with (a) Sentinel-1A SAR measurements, (b) the combine satellite and aircraft analysis, and (c) given in the Best-Track. Sentinel-1A-based wind structure is from quasi-instantaneous analysis measurements acquired between 10:29:51 UTC and 10:31:27 UTC, while the two others are based on measurements and data collected during 6 hr. The color code has been selected to specifically highlight the 34-, 50-, and 64-knot wind radii. Note that in (a), Sentinel-1A wind structure has been relocated to the exact storm location used for the two other analyses. Black box indicates the original SAR coverage. SAR = synthetic aperture radar.

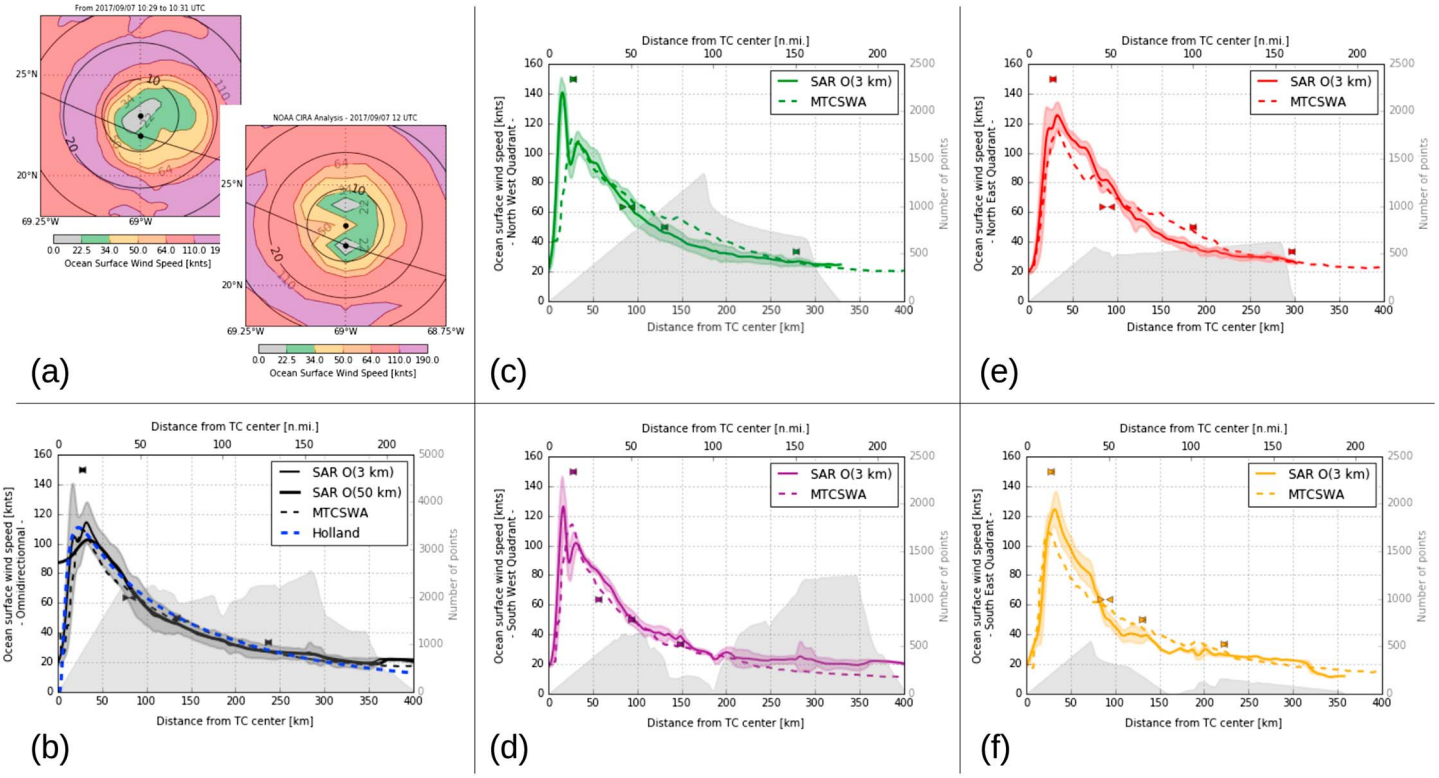

Figure 6. Irma ocean surface wind profiles with SAR observation and multiple satellite platform analysis. (a) Zoom of the wind structure obtained by the two approaches. (b) Omnidirectional ocean surface wind profile as a function of distance from the hurricane center up to 400 km. ">" and "<" indicate 34-, 50- and 64-knot wind radii given by the Best-Track analysis before and after Sentinel-1A acquisition time. Solid black line stands for SAR analysis (see legend for resolution) and dashed black line for multiple satellite platform analysis. Dashed line is the result given by Holland model. (c, d, e, and f) Same as for (b) but for the four geographical quadrants (NW, SW, SE, and NW). SAR = synthetic aperture radar; MTCSWA = Multi-observation Tropical Cyclone Surface Wind analysis.

Comparisons to quality controlled SFMR wind speeds tend to endorse these high wind speed estimates, which are not included in the MTCSWA.

Thus, within the inner core region, SAR measurements quite uniquely provide essential means to derive information in the vicinity of the eyewall. As anticipated for a category 5 TC, the SAR-derived maximum wind speed and the one-dimensional wind speed profile (solid black in Figure 1b) are very well approximated

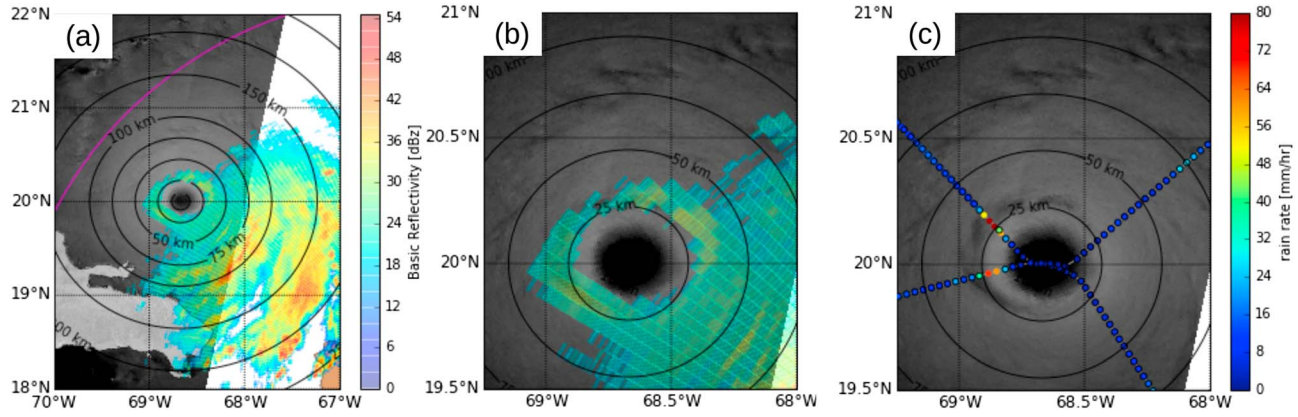

Figure 7. Rain during Irma category 5 hurricane on 7 September 2017. (a) SAR cross-polarized normalized radar cross section and base reflectivity measured NEXRAD at the same time. Purple line indicates the limit of NEXRAD coverage. (b) Zoomed on Irma eye. (c) Same as (b) but the color code indicates rain rate measured by SFMR. Circles with (respectively, without) black contours are considered as good (respectively, bad) SFMR data as indicated by the product quality flag. SAR = synthetic aperture radar; NEXRAD = Next-Generation Radar; SFMR = Stepped Frequency Microwave Radiometer.

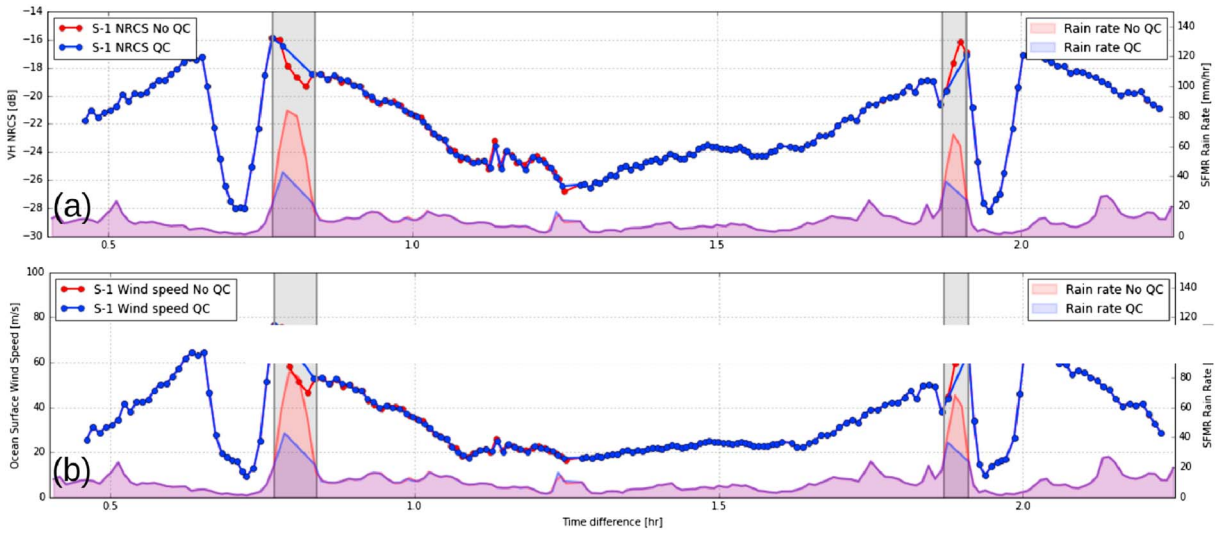

Figure 8. Impact of rain on SAR measurement near the maximum wind speed area. (a) Transect of SAR cross-polarized normalized radar cross section (NRCS) and (b) SAR-derived ocean surface wind speed collocated with SFMR at 3-km resolution. Solid blue (respectively, red) lines are measurements obtained after collocation when a (respectively, no) filtering of the data with respect to the quality flag in SFMR products is applied. SAR = synthetic aperture; SFMR = Stepped Frequency Microwave Radiometer. radar

using a parametric Holland model (dashed blue line in Figure 1b). Combined with the pressure of the outermost closed isobar given by the Best-Track, it yields a central surface pressure of 918 hPa. Remarkably, this estimate of the central surface pressure almost perfectly coincides with the 921-hPa value, as given by the Best-Track and based on aircraft reconnaissance. The analysis of the two-dimensional wind structure further provides some asymmetrical descriptors (e.g., Zhang et al., 2017), including for each quadrant or azimuth direction, the corresponding maximum wind speed and its associated radius, but also the full wind gradient (dV/dr) profile. For the present Irma case study, in the direction of the maximum wind speed, a 64-m/s increase in less than 10 km is obtained, to correspond to an absolute vorticity of $210f$, where f is the Coriolis parameter, within the inner core.

3.3.2. Rain Impact

As a short-microwave active radar instrument, C-Band SAR signals can be affected by rain. Typically, it has been reported (Tournadre & Quilfen, 2003, 2005) that intense rain reduces the Ku-band QuikSCAT retrieved wind speed by about 5 m/s for rain rate 10 mm/hr and wind speed 30 m/s. Thanks to their dual-frequency capability (Ku- and C-band), altimeters signals have also been jointly processed using adapted algorithms (Quilfen et al., 2006, 2010) to retrieve surface wind/wave information, along with the rain rate in extreme weather events. Compared to Ku-band, C-band data were reported to be far less affected by rain. For a maximum attenuation of 10 dB for the Ku-band instrument, the attenuation at C-band is only 1 dB, in line with Marshall-Palmer relationships (Marshall & Palmer, 1948). For off-nadir measurements, this rain impact on C-band measurements has already been addressed in the literature, especially under moderate wind speeds. In particular, first studies documented rain cell signatures associated with downdraft (Atlas, 1994a, 1994b). Although not necessarily strongly attenuated, C-band SAR images often clearly imprint rain events, including diverse forms such as stratified rain, rain bands, and squall lines (Alpers et al., 2016). But, as backscatter signals are usually only slightly hampered, and not fully attenuated to be easily flagged, these different analyses report very well the challenges to face for an accurate interpretation of rain effects at C-band.

It is likely that raindrops impinging onto the sea surface can affect the backscattered radar power. In the particular case of very high rain rates (above 40 mm/hr), both scattering from hydrometeors at the melting layer and attenuation of the radar signal by rain drops in the atmosphere coexist (see Figure 3(a) from Alpers et al., 2016, with C-Band data acquired over the rain forest). In addition, the importance of these different effects is likely dependent on the background sea state and surface roughness. To note, rain signatures at high resolution often consist as adjacent areas of both enhanced and reduced NRCS values (relative to the ambient rain-free and downdraft-free area). For rain signatures detected from C-Band SAR images acquired over TCs, RADARSAT-1 images in copolarization, together with coastal rain radar and radiometer measurements, have already been discussed (Katsaros et al., 2000) and then further documented (Li et al.,

2013). As concluded, attenuated and enhanced backscattered signals coexist in TC SAR images. But, to date, lack of dedicated investigations preclude definite conclusions. Most studies remain insufficiently documented with few reference concurrent data (including rain, wind, and sea state), and no systematic and robust methods exist to possibly correct effects in SAR images.

In the present study, the NEXRAD rain radar (IJUA) located in Puerto Rico was still operating when Irma approached the Dominican Republic. We can thus use NEXRAD base reflectivity measurements and take advantage of its very high temporal resolution. A base reflectivity map collocated with SAR acquisition is presented in Figure 7a. A zoom in on the TC eye is shown in Figure 7b. In Figure 7a, the purple line is the limit of the NEXRAD radar field of view. NEXRAD radar measurements indicate that more rain occurred on the east side of the storm. In contrast, NEXRAD reflectivity is absent in the western part of the storm, corresponding apparently to a less rainy area. A clear 5-km ring rain is observed around the TC eye at about 30–35 km (about 15–20 n.mi) from the TC center. For the western part of the TC, the accuracy of the NEXRAD is questionable as the TC is close to its field of view limit. The obtained reflectivity map differs significantly from measurements when the TC was very close to Puerto Rico on 6 September (see NHC report). Collocated SAR measurements and rain rates measured from SFMR along the flight are also available and superimposed to the SAR image intensity in Figure 7c. Measurements that are considered as good (respectively, bad) quality in the SFMR product are indicated by circles with (respectively, without) black contours. SFMR measurements indicate high-quality rain rates up to 40 mm/hr around the TC eye in agreement with NEXRAD high reflectivity. In addition, we also note rain rates around 30 mm/hr in the NE quadrant ($R \approx 75$ km; about 40 n.mi) and 20 mm/hr in the NW quadrant ($R \approx 70$ km; about 38 n.mi) corresponding to visible and narrow rain bands in SAR image.

Around the TC eye, where significant rain rates are detected by both NEXRAD and SFMR, Sentinel-1 NRCS signals display a general attenuation. To get a quantitative assessment of this intensity loss, Sentinel-1 NRCS are collocated with SFMR, without and with the SFMR product quality control criteria applied. As observed in Figures 8a and 8b, during the first transect across Irma TC eye ($\Delta T \approx 0.8$ hr, i.e., 50 min), a signal drop of about 2 dB is found for the NRCS in the area associated with high rain rate (NW area). The comparison obtained during the second transect ($\Delta T \approx 1.9$ hr, i.e., 1 hr and 55 min) shows an increase. It is noteworthy that, and as already pointed out in the previous section, this apparent inconsistency between these two comparisons is, to a large extent, attributed to the relative inaccuracy of our collocation method. This certainly confirms the inherent limitation of collocating airborne and spaceborne measurements, especially considering very high resolution data. If more carefully and manually corrected, to best align NRCS profile and SFMR wind profile, a 1.5-dB decrease is found for the NRCS in the area associated with high rain rate. It is noteworthy that in these two particular cases the nonqualified rain rates are about 80 and 60 mm/hr, respectively. This suggests very extreme rain rate conditions. Accordingly, close to the TC eyes, where very intense rain occurs, a significant decrease of the NRCS is observed. Note that it applies to both copolarized and cross-polarized signals (not shown). These results agree with the typical location of eyewall rainfall as discussed in Jorgensen (1984).

At this stage, there is not enough evidence to conclude if these overall signal changes are solely due to rain impacts, to wind changes, or to their combined effects. As computed with the proposed wind retrieval algorithm, the resulting localized decrease of the estimated ocean surface wind speed corresponds to about 5–10 m/s near the hurricane maximum wind speed (~75 m/s) area. As shown and detected as the dark circular shape in Figure 7, visible impacts cover almost all the western part of the TC eye, at a distance of about 30–35 km (15–20 n.mi), and over a relatively limited width of about 5 km. As such, this naturally induces apparent double rings on the wind speed map (see Figure 4a). This also explains the trend of the wind field profiles obtained in NW and SW quadrants at this radius (see Figure 6).

4. Conclusions and Perspectives

Following previously reported studies, the present analysis fully confirms the potential to quantitatively interpret, at very high resolution, the sea surface imprints captured by spaceborne SAR measurements under extreme weather conditions. Specifically, the combined copolarized and cross-polarized signals provide unique high-resolution and nearly instantaneous views of the expected intense and rapidly evolving interactions, occurring near the ocean surface. In these extreme hurricane conditions, heavy precipitation, clouds, and high values of water vapor content combine to significantly mask the ocean contribution to

high-frequency microwave brightness temperatures and Vis-IR measurements. Least affected under extreme environmental conditions, lower-frequency satellite-borne passive microwave instruments (e.g., Reul et al., 2012, 2017; Zabolotskikh et al., 2013), do not operate at sufficient spatial resolution. Quantitatively interpreted, imaging radar systems can thus offer new independent means to complement existing observing systems, with very high resolution O(1 km) description of the TC ocean boundary layer structures. SAR backscatter signals have generally sufficient sensitivity to precisely map surface wind structures in and around the TC eyes, as demonstrated in the present investigation. More specifically for cross-polarization measurements, the radar intensity emerge well above noise and remains significantly sensitive to infer ocean surface information for category 5 hurricanes, with wind speeds reaching up to 75 m/s, as also estimated by SFMR local measurements.

Our conclusions apply to both Radarsat-2 and Sentinel-1 SAR missions. The remarkable consistency between the two missions is obtained after considering proper noise correction. Findings indicate noise correction is an absolute necessity and an essential aspect of processing SAR data. It primarily helps the geophysical interpretation to further pave the way for a combined use of these missions to improve the spatio-temporal coverage for hurricane monitoring. Currently, with three SAR systems operating in copolarization and cross-polarization, and possibly four with Gaofeng-3, a dedicated acquisition strategy could be defined, such as to ensure that a particular TC would be followed throughout its life cycle. Combined with medium resolution observations (e.g., Reul et al., 2017; Zhao et al., 2018), this would certainly provide unprecedent observations to both quantify high-resolution air-sea interactions and describe the organized wind structures during intensification mature and weakening phases.

In this study, the two polarized (copolarized and cross-polarized) signals are combined. This helps to retrieve ocean surface wind speeds at 3-km resolution. In the Irma case study presented here, the resulting wind estimates are found to be in very close agreement with collocated SFMR measurements. The overall bias is about 1.5 m/s, standard deviation around 5 m/s, and correlation coefficient higher than 90%. The large SAR swath also provides the 2-D structure of the wind over hundreds of kilometers. Accordingly, this synoptic capacity is directly used to infer typical TC structure parameters, routinely derived by operational hurricane centers. Again, the SAR-derived parameters are found to be in line with those provided by operational hurricane centers. This certainly suggests the potential for SAR winds to aid existing operational methodologies, already relying on various available data, to infer practical and essential TC parameters: precise wind radii and the degree of storm symmetry. SAR-derived TC information can also be used to help constrain theoretically based parametric wind models and possibly to inform forecasters about inner core processes that could possibly lead to improved intensity forecasts.

The precise analysis of high-resolution data has also limitations. At first, the collocation method, classically used to analyze radar parameters or radar-derived geophysical parameters, certainly needs to be revisited. Indeed, in the case of major hurricanes, such as the Irma case study analyzed in section 3, extreme gradients occur within the eyewall. Using high-resolution SAR images, a small shift in the collocation can then lead to strong misalignment between measurements and huge impacts on direct comparisons. Not only the proposed relationship could certainly benefit for more measurements, but this shall be further constrained using more severe criteria for collocations ($\Delta T \leq$ 30min). As foreseen, necessary future studies shall be devoted to improve the quality control of SAR data, to again augment comparisons with reference measurements, especially including ocean surface wind speed and also surface waves and subsurface currents (Mitarai & McWilliams, 2016).

Moreover, heavy and very localized rainfalls around the eye are also important to consider and possibly monitor using high-resolution SAR measurements. An automated flag for the rain in these situations, to trace and possibly compare radar signatures with high-frequency microwave brightness temperature measurements, would be beneficial, especially to help characterize the rain structures in the inner core and near maximum wind areas. Local gradient analysis developed by Koch (2004) have already been applied to hurricanes (Horstmann et al., 2013; Mouche et al., 2017). Very localized rain events in Irma, as detected using collocated ground-based rain-radar reflectivity measurements, lead to strong variations in the radar signals, translating to 5–10 m/s changes in less than tens of kilometers. Alternating radar intensity variations can then produce double-ring effects on the retrieved wind speed field. Yet, to date, it is not possible to unambiguously estimate and separate the contributions of precipitation from those associated to winds.

Acknowledgments
The SHOC initiative has been possible thanks to SAR data access supported by ESA Sentinel-1 mission ground segment team and GIS BreTel. In particular, the implication of L. Martino, P. Potin, Y.-L. Desnos, and M. Engdhal at ESA and the whole Sentinel-1 mission planning team has been decisive. Authors also acknowledge Joe Sapp (NOAA/NESDIS) for SFMR data, R. Husson (CLS) and F. Said (NOAA/NESDIS) for technical support during SHOC in summer 2017, K. Cordier (CLS) and N. Franceschi (Aresys) from Sentinel-1 Mission Performance Center for providing Irma data processed with IPF 2.90, Nuno Miranda (ESA) for support with Sentinel-1 data, and Olivier Archer (IFREMER) for his mastering of Nephelea computer system. This study contains modified Copernicus Sentinel-1 (2016-2018) and RADARSAT-2 data. Sentinel-1 is part of the European space component of Copernicus European program. Data are free of charge and available on the Copernicus Open Access Hub (https://scihub.copernicus.eu/). RADARSAT-2 is a commercial mission, and data are provided by MDAs Geospatial Services (https://mdacorporation.com/geospatial/international). Access to RADARSAT-2 data was supported by public funds (Ministère de l'Education Nationale, de l'Enseignement Supérieur et de la Recherche, FEDER, Région Bretagne, Conseil Général du Finistère, Brest Métropole) and by Institut Mines Télécom, received in the framework of the VIGISAT project managed by "Groupement Bretagne Télédétection" (GIS BreTel Brittany Remote Sensing). The NEXRAD and hurricane track products are archived by the National Climatic Data Center and available via FTP download (http://www.ncdc.noaa.gov/nexradinv/choosesite.jsp) and IBTrACS website (https://www.ncdc.noaa.gov/ibtracs/). SFMR and combined satellite aircraft analysis products are provided by NOAA/NESDIS team respectively at https://manati.star.nesdis.noaa.gov/SFMR/1.0/ and http://rammb.cira.colostate.edu/products/tc_realtime/index.asp websites. This work was partly supported by CNES TOSCA program (COWS project), by European Space Agency through S1-4SCI Ocean Study project (contract 4000115170/15/I-SBo), Sentinel-1 A Mission Performance Center (contract 4000107360/12/I-LG), EUMETSAT CHEF project, ANR (FEM) CARAVELE project, National Science Foundation of China for outstanding Young Scientist under grant 41622604, and in part by the Excellent Youth Science Foundation of Jiangsu

Further investigations, possibly building on available rain radar measurements, and SFMR rain estimates, are beyond the scope of this present paper but will be considered in near future studies. In particular, efforts will be dedicated to evaluate and document the possible differing polarization sensitivity to heavy precipitations. Finally, the combination of SAR measurements with parametric TC wind model has already proven to be useful to overcome SAR limitations such as saturation of the signal in copolarization (Reppucci et al., 2010) but also rain attenuation (Zhang et al., 2017). Although applied to a limited data set with wind speeds lower than or equal to 40 m/s, this method is certainly one way to flag of heavy precipitation.

To conclude, the continuation of routine acquisition of SAR data over TCs and creation of wind speed estimates database would fulfill both research and operational needs. While operational centers are required to estimate the extent of 34-, 50- and 64-knot (17, 25, and 33 m/s, respectively) winds, and the RMW, in reality there are very few observational platforms that can provide accurate assessments of metrics associated with higher wind speeds (e.g., above 50 knots or 25 m/s). And in the absence of aircraft reconnaissance and/or a clearly defined satellite eye, the RMW is typically no more than an educated guess. Theses platforms include scatterometers, aircraft reconnaissance, microwave sounder-based techniques, and multiplatform techniques, but each has their shortcomings. Scatterometer-based winds begin to saturate above 25 m/s, aircraft reconnaissance is rarely available, microwave sounders suffer from low spatial resolutions, and attenuation and scattering in precipitating scenes and multi-platform techniques rely heavily on statistical proxies for the winds based on infrared imagery. The existing SHOC data set is also a gold mine of information to be further explored for research, providing unique nearly instantaneous views of TC of all intensities and in all the global basins. Research and applied research communities can used these data for developing and testing models and multisensor techniques to better estimate structural features, particularly 64- and 100-knot wind radii, and the RMW.

The location of the RMW, particularly for systems without an eye feature, is particularly difficult to estimate from the current space-based observing platforms. Its location is however very important. RMW is a key parameter in many parametric vortex models (Deppermann, 1947; Holland, 1980; Holland et al., 2010; Willoughby & Rahn, 2004; Wood & White, 2011), and these models are routinely used to derive storm surge and risk models (Lin & Chavas, 2012, and references therein). In addition, the location of the RMW with respect to convective heating has been shown to influence the response of the TC secondary circulation (Schubert & Hack, 1982) and thus is potentially important for the short-term forecasting of intensity change (Carrasco et al., 2014; Wang et al., 2015). Finally, SAR data could be used to study, in detail, the existence and formation of secondary eyewall features and eyewall replacement cycles (see Kossin & Sitkowski, 2009and references within), which are often monitored using ice scattering signals from microwave imagers. Adopting a clear and sustainable strategy for SAR acquisitions over TC is thus a key point to further secure research and operational activities.

References

Alpers, W., Zhang, B., Mouche, A., Zeng, K., & Chan, P. W. (2016). Rain footprints on C-band synthetic aperture radar images of the ocean—Revisited. *Remote Sensing of Environment*, *187*, 169–185. https://doi.org/10.1016/j.rse.2016.10.015

Atlas, D. (1994a). Footprints of storms on the sea: A view from spaceborne synthetic aperture radar. *Journal of Geophysical Research*, *99*(C4), 7961–7969. https://doi.org/10.1029/94JC00250

Atlas, D. (1994b). Origin of storm footprints on the sea seen by synthetic aperture radar. *Science*, *266*(5189), 1364–1366.

Banal, S., Iris, S., & Saint-Jean, R. (2007). Canadian Space Agency hurricane watch program: Archive contents, data access and improved planning strategies. In *Proceeding of IEEE International Geoscience and Remote Sensing Symposium* (pp. 3494–3497). Barcelona, Spain. https://doi.org/10.1109/IGARSS.2007.4423599

Barnes, S. L. (1964). A technique for maximizing details in numerical weather map analysis. *Journal of Applied Meteorology*, *3*(4), 396–409. https://doi.org/10.1175/1520-0450(1964)003<0396:ATFMDI>2.0.CO;2

Cangialosi, P., Latto, A. S., & Berg, R. (2018). NHC tropical cyclone report. Hurricane irma (AL112017 2016). Miami, FL: National Hurricane Center.

Carrasco, C. A., Landsea, C. W., & Lin, Y. L. (2014). The influence of tropical cyclone size on its intensification. *Weather and Forecasting*, *29*(3), 582–590. https://doi.org/10.1175/WAF-D-13-00092.1

Deppermann, C. E. S. J. (1947). Notes on the origin and structure of Philippine typhoons. *Bulletin of the American Meteorological Society*, *28*(9), 399–404. https://doi.org/10.1175/1520-0477-28.9.399

Federal Meteorological Handbook No. 11—Doppler Radar meteorological observations (WSR-88D). Part C: WSR-88D products and algorithms (2017) (*FCM-H11C-2017*). Silver Spring, MD: Office of the federal coordinator for meteorological services and supporting research.

Fois, F., Hoogeboom, P., Le Chevalier, F., Stoffelen, A., & Mouche, A. (2015). DopSCAT: A mission concept for simultaneous measurements of marine winds and surface currents. *Journal of Geophysical Research: Oceans*, *120*, 7857–7879. https://doi.org/10.1002/2015JC011011

Franklin, J. L., Black, M. L., & Valde, K. (2003). GPS dropwindsonde wind profiles in hurricanes and their operational implications. *Weather and Forecasting*, *18*(1), 32–44. https://doi.org/10.1175/1520-0434(2003)018<0032:GDWPIH>2.0.CO;2

province under grant BK2016090. Knaff is supported by NOAA NESDIS base funding. The views, opinions, and findings contained in this report are those of the authors and should not be construed as an official NOAA or U.S. Government position, policy, or decision.

Fu, L. L., & Holt, B. (1982). Seasat views oceans and sea ice with synthetic-aperture radar. USA: Jet Propulsion Laboratory.

Holland, G. J. (1980). An analytic model of the wind and pressure profiles in hurricanes. *Monthly Weather Review*, *108*(8), 1212–1218. https://doi.org/10.1175/1520-0493(1980)108<1212:AAMOTW>2.0.CO;2

Holland, G. J., Belanger, J. I., & Fritz, A. (2010). A revised model for radial profiles of hurricane winds. *Monthly Weather Review*, *138*(12), 4393–4401. https://doi.org/10.1175/2010MWR3317.1

Horstmann, J., Thompson, D. R., Monaldo, F., Iris, S., & Graber, H. C. (2005). Can synthetic aperture radars be used to estimate hurricane force winds? *Geophysical Research Letters*, *32*, L22801. https://doi.org/10.1029/2005GL023992

Horstmann, J., Wackerman, C., Falchetti, S., & Maresca, S. (2013). Tropical cyclone winds retrieved from synthetic aperture radar. *Oceanography*, 46–57. https://doi.org/10.5670/oceanog.2013.30

Hwang, P., Stoffelen, A., van Zadelhoff, G. J., Perrie, W., Zhang, B., Li, H., & Shen, H. (2015). Cross-polarization geophysical model function for C-band radar backscattering from the ocean surface and wind speed retrieval. *Journal of Geophysical Research: Oceans*, *120*, 893–909. https://doi.org/10.1002/2014JC010439

Jorgensen, D. F. (1984). Mesoscale and convective-scale characteristics of mature hurricanes. Part I: General observations by research aircraft. *Journal of the Atmospheric Sciences*, *41*(8), 1268–1286. https://doi.org/10.1175/1520-0469(1984)041<1268:MACSCO>2.0.CO;2

Katsaros, K. B., Vachon, P. W., Black, P. G., Dodge, P. P., & Ulhorn, E. W. (2000). Wind fields from SAR: Could they improve our understanding of storm dynamics? *Johns Hopkins APL Technical Digest (Applied Physics Laboratory)*, *21*(1), 86–93.

Klotz, B. W., & Uhlhorn, E. W. (2014). Improved stepped frequency microwave radiometer tropical cyclone surface winds in heavy precipitation. *Journal of Atmospheric and Oceanic Technology*, *31*(11), 2392–2408. https://doi.org/10.1175/JTECH-D-14-00028.1

Knaff, J. A., DeMaria, M., Molenar, D. A., Sampson, C. R., & Seybold, M. G. (2011). An automated, objective, multiple-satellite-platform tropical cyclone surface wind analysis. *Journal of Applied Meteorology and Climatology*, *50*(10), 2149–2166. https://doi.org/10.1175/2011JAMC2673.1

Knaff, J. A., Longmore, S. P., DeMaria, R. T., & Molenar, D. A. (2015). Improved tropical-cyclone flight-level wind estimates using routine infrared satellite reconnaissance. *Journal of Applied Meteorology and Climatology*, *54*(2), 463–478. https://doi.org/10.1175/JAMC-D-14-0112.1

Knapp, K. R., Kruk, M. C., Levinson, D. H., Diamond, H. J., & Neumann, C. J. (2010). The International Best Track Archive for Climate Stewardship (IBTrACS). *Bulletin of the American Meteorological Society*, *91*(3), 363–376. https://doi.org/10.1175/2009BAMS2755.1

Koch, W. (2004). Directional analysis of SAR images aiming at wind direction. *IEEE Transactions on Geoscience and Remote Sensing*, *42*, 702–710. https://doi.org/10.1109/TGRS.2003.818811

Koch, S. E., desJardins, M., & Kocin, P. J. (1983). An interactive Barnes objective map analysis scheme for use with satellite and conventional data. *Journal of Climate and Applied Meteorology*, *22*(9), 1487–1503. https://doi.org/10.1175/1520-0450(1983)022<1487:AIBOMA>2.0.CO;2

Kossin, J. P., & Sitkowski, M. (2009). An objective model for identifying secondary eyewall formation in hurricanes. *Monthly Weather Review*, *137*(3), 876–892. https://doi.org/10.1175/2008MWR2701.1

Kruk, M. C., Knapp, K. R., & Levinson, D. H. (2010). A technique for combining global tropical cyclone best track data. *Journal of Atmospheric and Oceanic Technology*, *27*(4), 680–692. https://doi.org/10.1175/2009JTECHA1267.1

Kudryavtsev, V. N., Chapron, B., Myasoedov, A. G., Collard, F., & Johannessen, J. A. (2013). On dual co-polarized SAR measurements of the ocean surface. *IEEE Geoscience and Remote Sensing Letters*, *10*(4), 761–765. https://doi.org/10.1109/LGRS.2012.2222341

Kudryavtsev, V., Kozlov, I., Chapron, B., & Johannessen, J. A. (2014). Quad-polarization SAR features of ocean currents. *Journal of Geophysical Research: Oceans*, *119*, 6046–6065. https://doi.org/10.1002/2014jc010173

Landsea, C. W., & Franklin, J. L. (2013). Atlantic hurricane database uncertainty and presentation of a new database format. *Monthly Weather Review*, *141*(10), 3576–3592. https://doi.org/10.1175/MWR-D-12-00254.1

Li, X., Zhang, J. A., Yang, X., Pichel, W. G., Demaria, M., Long, D., & Li, Z. (2013). Tropical cyclone morphology from spaceborne synthetic aperture radar. *Bulletin of the American Meteorological Society*, *94*(2), 215–230. https://doi.org/10.1175/BAMS-D-11-00211.1

Lin, N., & Chavas, D. (2012). On hurricane parametric wind and applications in storm surge modeling. *Journal of Geophysical Research*, *117*, D09120. https://doi.org/10.1029/2011JD017126

Marshall, J., & Palmer, W. (1948). The distribution of raindrops with size. *Journal of Meteorology*, *5*, 165–166.

Meissner, T., Ricciardulli, L., & Wentz, F. (2017). Capability of the SMAP mission to measure ocean surface winds in storms. *Bulletin of the American Meteorological Society*, *98*(8), 1660–1677. https://doi.org/10.1175/BAMS-D-16-0052.1

Miller, R. J., Schrader, A. J., Sampson, C. R., & Tsui, T. L. (1990). The automated tropical cyclone forecasting system (ATCF). *Weather and Forecasting*, *5*(4), 653–660. https://doi.org/10.1175/1520-0434(1990)005<0653:TATCFS>2.0.CO;2

Miranda, N., Recchia, A., Franceschi, N., Piantanida, R., Meadows, P., & Mouche, A. (2017). Sentinel-1 new (thermal) denoising approach, *CEOS workshop on calibration and validation—Synthetic aperture radar subgroup*. Pasadena, CA: Jet Propulsion Laboratory, California Institute of Technology.

Mitarai, S., & McWilliams, J. C. (2016). Wave glider observations of surface winds and currents in the core of Typhoon Danas. *Geophysical Research Letters*, *43*, 11,312–11,319. https://doi.org/10.1002/2016GL071115

Mouche, A., & Chapron, B. (2015). Global C-band Envisat, RADARSAT-2 and Sentinel-1 SAR measurements in copolarization and cross-polarization. *Journal of Geophysical Research: Oceans*, *120*, 7195–7207. https://doi.org/10.1002/2015JC011149

Mouche, A., Chapron, B., Zhang, B., & Husson, R. (2017). Combined co- and cross-polarized SAR measurements under extreme wind conditions. *IEEE Xplore: IEEE Transactions on Geoscience and Remote Sensing*, *55*, 6476–6755.

Mouche, A. A., Collard, F., Chapron, B., Dagestad, K. F., Guitton, G., Johannessen, J. A., et al. (2012). On the use of Doppler shift for sea surface wind retrieval from SAR. *IEEE Transactions on Geoscience and Remote Sensing*, *50*(7), 2901–2909. https://doi.org/10.1109/TGRS.2011.2174998

Piantanida, R., Miranda, N., & Franceschi, N. (2017). Thermal denoising of products generated by the S-1 IPF. Sentinel-1 Mission Performance Centre Technical Document. Retrieved from https://sentinel.esa.int/documents/247904/2142675/Thermal-Denoising-of-Products-Generated-by-Sentinel-1-IPF

Quilfen, Y., Chapron, B., & Tournadre, J. (2010). Satellite microwave surface observations in tropical cyclones. *Monthly Weather Review*, *138*(2), 421–437. https://doi.org/10.1175/2009MWR3040.1

Quilfen, Y., Tournadre, J., & Chapron, B. (2006). Altimeter dual-frequency observations of surface winds, waves, and rain rate in Tropical Cyclone Isabel. *Journal of Geophysical Research*, *111*, C01004. https://doi.org/10.1029/2005JC003068

Rappaport, E. N., Franklin, J. L., Avila, L. A., Baig, S. R., Beven, J. L., Blake, E. S., et al. (2009). Advances and challenges at the National Hurricane Center. *Weather and Forecasting*, *24*(2), 395–419. https://doi.org/10.1175/2008WAF2222128.1

Reppucci, A., Lehner, S., Schulz-Stellenfleth, J., & Brusch, S. (2010). Tropical cyclone intensity estimated from wide-swath SAR images. *IEEE Transactions on Geoscience and Remote Sensing*, *48*(4), 1639–1649. https://doi.org/10.1109/TGRS.2009.2037143

Reul, N., Chapron, B., Zabolotskikh, E., Donlon, C., Mouche, A., Tenerelli, J., et al. (2017). A new generation of tropical cyclone size measurements from space. *Bulletin of the American Meteorological Society*, *98*(11), 2367–2385. https://doi.org/10.1175/BAMS-D-15-00291.1

Reul, J., Tenerelli, J., Chapron, B., Vandemark, D., Quilfen, Y., & Kerr, Y. (2012). SMOS satellite L-band radiometer: A new capability for ocean surface remote sensing in hurricanes. *Journal Of Geophysical Research*, *117*, C02006. https://doi.org/10.1029/2011JC007474

Sampson, C. R., Goerss, J. S., Knaff, J. A., Strahl, B. R., Fukada, E. M., & Serra, E. A. (2018). Tropical cyclone gale wind radii estimates, forecasts, and error forecasts for the western North Pacific. *Weather and Forecasting*, *33*(4), 1081–1092. https://doi.org/10.1175/WAF-D-17-0153.1

Sampson, C. R., & Schrader, A. J. (2000). The automated tropical cyclone forecasting system (version 3.2). *Bulletin of the American Meteorological Society*, *81*(6), 1231–1240. https://doi.org/10.1175/1520-0477(2000)081<1231:TATCFS>2.3.CO;2

Schreck, C. J., Knapp, K. R., & Kossin, J. P. (2014). The impact of best track discrepancies on global tropical cyclone climatologies using IBTrACS. *Monthly Weather Review*, *142*(10), 3881–3899. https://doi.org/10.1175/MWR-D-14-00021.1

Schubert, W. H., & Hack, J. J. (1982). Inertial stability and tropical cyclone development. *Journal of the Atmospheric Sciences*, *39*(8), 1687–1697. https://doi.org/10.1175/1520-0469(1982)039<1687:ISATCD>2.0.CO;2

Stoffelen, A., Aaboe, S., Calvet, J. C., Cotton, J., De Chiara, G., Saldana, J., et al. (2017). Scientific developments and the EPS-SG scatterometer. *IEEE Journal Of Selected Topics In Applied Earth Observations And Remote Sensing*, *10*(5), 2086–2097.

Tournadre, J., & Quilfen, Y. (2003). Impact of rain cell on scatterometer data: 1. Theory and modeling. *Journal of Geophysical Research*, *108*(C7), 3225. https://doi.org/10.1029/2002JC001428

Tournadre, J., & Quilfen, Y. (2005). Impact of rain cell on scatterometer data: 2. Correction of seawinds measured backscatter and wind and rain flagging. *Journal of Geophysical Research*, *110*, NIL_32–NIL_47. https://doi.org/10.1029/2002JC001428

Uhlhorn, E. W., & Black, P. G. (2003). Verification of remotely sensed sea surface winds in hurricanes. *Journal of Atmospheric and Oceanic Technology*, *20*(1), 99–116. https://doi.org/10.1175/1520-0426(2003)020<0099:VORSSS>2.0.CO;2

Uhlhorn, E. W., Black, P. G., Franklin, J. L., Goodberlet, M., Carswell, J., & Goldstein, A. S. (2007). Hurricane surface wind measurements from an operational stepped frequency microwave radiometer. *Monthly Weather Review*, *135*(9), 3070–3085. https://doi.org/10.1175/MWR3454.1

Wang, Y., Rao, Y., Tan, Z. M., & Schönemann, D. (2015). A statistical analysis of the effects of vertical wind shear on tropical cyclone intensity change over the western North Pacific. *Monthly Weather Review*, *143*(9), 3434–3453. https://doi.org/10.1175/MWR-D-15-0049.1

Willoughby, H. E., & Rahn, M. E. (2004). Parametric representation of the primary hurricane vortex. Part I: Observations and evaluation of the Holland (1980) model. *Monthly Weather Review*, *132*(12), 3033–3048. https://doi.org/10.1175/MWR2831.1

Wood, V. T., & White, L. W. (2011). A new parametric model of vortex tangential-wind profiles: Development, testing, and verification. *Journal of the Atmospheric Sciences*, *68*(5), 990–1006. https://doi.org/10.1175/2011JAS3588.1

Yueh, S., Fore, A., Tang, W., Akiko, H., Stiles, B., Reul, N., et al. (2016). SMAP L-band passive microwave observations of ocean surface wind during severe storms. *IEEE Transactions on Geoscience and Remote Sensing*, *54*(12), 7339–7350.

Zabolotskikh, E. V., Mitnik, L. M., & Chapron, B. (2013). New approach for severe marine weather study using satellite passive microwave sensing. *Geophysical Research Letters*, *40*, 3347–3350. https://doi.org/10.1002/grl.50664

Zhang, G., Li, X., Perrie, W., Hwang, P. A., Zhang, B., & Yang, X. (2017). A hurricane wind speed retrieval model for C-band RADARSAT-2 cross-polarization ScanSAR images. *IEEE Transactions on Geoscience and Remote Sensing*, *55*, 4766–4774.

Zhang, B., & Perrie, W. (2012). Cross-polarized synthetic aperture radar: A new potential technique for hurricanes. *Bulletin of the American Meteorological Society*, *93*, 531–541.

Zhang, J. A., & Uhlhorn, E. W. (2012). Hurricane sea surface inflow angle and an observation-based parametric model. *Monthly Weather Review*, *140*(11), 3587–3605. https://doi.org/10.1175/MWR-D-11-00339.1

Zhao, Y., Mouche, A. A., Chapron, B., & Reul, N. (2018). Direct comparison between active C-band radar and passive L-band radiometer measurements: Extreme event cases. *IEEE Geoscience and Remote Sensing Letters*, *15*(6), 897–901. https://doi.org/10.1109/LGRS.2018.2811712